Journal of Materials Chemistry C

Improved efficiency of inverted planar perovskite solar cells with ultrahigh work function doped polymer as alternative hole transport layer

Journal:	*Journal of Materials Chemistry C*
Manuscript ID	TC-ART-10-2021-005072.R1
Article Type:	Paper
Date Submitted by the Author:	31-Jan-2022
Complete List of Authors:	Al-Dainy, Gailan; University of Arkansas at Little Rock Nima, Zeid; University of Arkansas at Little Rock, Center for Integrative Nanotechnology Sciences Hashoosh, Ahmed; University of Arkansas at Little Rock Watanabe, Fumiya; University of Arkansas at Little Rock, Center for Integrative Nanotechnology Sciences Biris, Alexandru; University of Arkansas, Nanotechnology Center, Applied Science Department Bourdo, Shawn; University of Arkansas at Little Rock, Center for Integrative Nanotechnology Sciences

Improved efficiency of inverted planar perovskite solar cells with ultrahigh work function doped polymer as alternative hole transport layer

Gailan A. Al-Dainy[a],*, Zeid N. Al Sudani[a], Ahmed Hashoosh[a], Fumiya Watanabe[a], Alexandru S. Biris[a],*, and Shawn E. Bourdo[a],*

[a] Center for Integrative Nanotechnology Sciences, University of Arkansas at Little Rock, 2801 S. University Ave., Little Rock, AR, 72204 (USA)

*Corresponding Authors: gaaldainy@ualr.edu, gaaldainy@gmail.com (GA Al-Dainy), asbiris@ualr.edu (AS Biris), and sxbourdo@ualr.edu (SE Bourdo)

Abstract

The solar energy field is in need of better inverted planar perovskite solar cells that feature proper energy level alignment, efficient carrier transport in the hole transport layers, and a high-quality perovskite film on top. To help meet this need, we have developed a new transparent conductive polymer, based on sulfonated poly(thiophene-3-[2-(2-methoxy-ethoxy) ethoxy]-2,5-diyl) (S-P3MEET), as an alternative hole transport layer for inverted triple-cation lead mixed-halide perovskite. The resulting perovskite solar cell device showed efficiency of 17.25%, an open-circuit voltage (V_{oc}) of 0.965 V, and a fill factor of 80%, with minimal hysteresis. However, the pristine S-P3MEET also had a work function (WF) of -4.98eV, which is low and needed improvement to make high energy level alignment at the perovskite interface. To overcome this drawback and make an ohmic contact at the perovskite interfaces, we tuned the WF of the pristine S-P3MEET by adding a desired weight ratio of a perfluorinated ionomer (PFI) to the S-P3MEET bland solution. The fluorinated S-P3MEET had a better WF of -5.45 eV, leading to remarkable improvement in the V_{oc} of the inverted perovskite solar cell device. The resulting device with 10% wt PFI doping ratio showed efficiency of 19.6% with a V_{oc} of 1.07 V. In contrast, the control device (poly(3,4-ethylenedioxythiophene):poly(styrene sulfonate) (PEDOT:PSS)) had lower efficiency, 14.97%, with higher hysteresis effects. Most importantly, the fluorinated S-P3MEET perovskite device showed long-term stability due to the unique hydrophobicity of the capping layer of rich doping PFI on the S-P3MEET surface.

1. Introduction

Organic-inorganic perovskite solar cells (PSCs) are gaining popularity as next-generation photovoltaics due to their unique optoelectronic properties, including long exciton diffusion length, high absorption coefficient, small exciton binding energy, tunable bandgap, and high carrier mobility[1–5]. PSC performance depends on the quality of the perovskite active layer and its interfacial charge transport layers. Controlling the formation of a high-quality perovskite absorber layer with strategically chosen transport layers results in suppression of carrier recombination and facilitates carrier injection at the device layers[6,7]. The charge transport layers are vital factors for PSC performance and stability[8]. To date, PSCs based on n-i-p configuration show the highest performance[9]. However, electron acceptors such as compact or mesoporous layers require high preparation temperatures (e.g., TiO_2) or suffer from hysteresis issues (e.g., SnO_2)[10–13]. Furthermore, pore-filling issues can arise in the active layers of mesoporous-based devices, which enhance the recombination processes in the PSCs[4]. In addition, the hole transport layer (HTL) 2,2',7,7'-Tetrakis (N,N-di-p-methoxyphenylamino)-9,9'-spirobifluorene (spiro-OMeTAD), which is often used with n-i-p configurations, decreases the lifetime of PSC devices due to its salt dopant effects[14].

In contrast, PSCs with inverted architecture can be fabricated at low temperatures with negligible device hysteresis[15–18]. Therefore, inverted PSCs have received more attention in tandem and flexible substrate applications[4]. However, inverted PSCs suffer from excessive voltage loss through non-radiative recombination[19–24], which limits their open-circuit voltage (V_{OC}), compared to n-i-p configuration[6,7,24]. In order to overcome this limitation, polymer-based HTLs have been developed to improve the performance of inverted perovskite devices; these HTLs require easier solution processing techniques, and their electrochemical properties are fairly easy to modulate[25–28]. The thiophene-based conducting polymer poly(3,4-ethylenedioxythiophene):poly(styrene sulfonate) (PEDOT:PSS) is often used as an HTL for organic and perovskite solar cell devices. However, PEDOT:PSS is hygroscopic and can reduce the solar cell's lifetime due to water uptake diffusing though the device layers[29]. A scanning tunneling microscopy study showed that PEDOT:PSS films have a phase-separated structure, resulting in anisotropic conductivity[30,31]. PEDOT:PSS films also have anisotropic optical properties due to their ordinary and extraordinary complex refractive index[32]. Furthermore, reports show that inverted PSCs based on PEDOT:PSS

provide low Voc and short circuit current density (Jsc) due to the mismatched work function between PEDOT:PSS and the perovskite energy level[33,34]. Therefore, several chemical modifications have been employed to improve the properties of PEDOT:PSS, such as perfluorinated ionomer[35,36], graphene oxide (PEDOT:GO) composite[34], urea treatment[21], blended imidazole[27,37], PEDOT:P(SS-co-TFPMA)[38], ethylene glycol with methanol morphology[39], and PEDOT:PSS-ammonia modified graphene oxide (GO:NH_3) double-layer[40]. To date, the highest PSC efficiency obtained from modified PEDOT:PSS is 18.8% with a Voc of 1.03V[21], which is still low compared to n-i-p configuration devices. Therefore, a new HTL with enhanced optoelectronic properties for inverted PSCs is required as an alternative for PEDOT:PSS.

The chemical structure of poly(thiophene-3-[2-(2-methoxy-ethoxy)ethoxy]-2,5-diyl) (S-P3MEET) mimics that of PEDOT:PSS[30,31]; however, the S-P3MEET polymer has never been taken into consideration as an HTL for inverted PSC devices. Herein, S-P3MEET was investigated as a new HTL for inverted planar triple-cation perovskite solar cells due to its self-doping ability, in which the polymer and its sulfonate moieties do not have phase separation like PEDOT:PSS HTLs do[31,41]. While S-P3MEET and PEDOT:PSS are both derivatives of polythiophene, S-P3MEET is self-doped by the sulfonate moieties that are linked to the thiophene rings, while PEDOT:PSS has the dopant poly(styrene sulfonate) (PSS) in solution[30,31]. To improve the alignment energy at the perovskite-S-P3MEET interface, we tuned the WF of S-P3MEET by adding a desirable weight ratio of PFI to the S-P3MEET solution. The optoelectronic and chemical properties of the pristine and doped S-P3MEET films were characterized to determine the best inverted planar triple-cation PSC device.

2. Results and discussion

2.1. Structure and morphology

The chemical structures of S-P3MEET, PFI, and PEDOT:PSS are shown in Figure 1a. To investigate the use of PFI as an additional dopant to S-P3MEET, x-ray photoelectron spectroscopy (XPS) depth profiling was performed on the 10wt% PFI-doped S-P3MEET/glass film, with etching times extended to 330 s to create different etching levels (5 sec for each level) (Figure 1b). The fluorine atom (F) intensity (binding energy 688.6 eV) was attributed to the fluorocarbon chains (CF_2) in PFI molecules that accumulated at the surface and decreased markedly within the bulk of the films. The self-segregation of PFI was driven by the migration of its low-surface energy

fluorinated chains to the surface, increasing the hydrophobicity of S-P3MEET[42,43]. The XPS narrow scans of the S(2p) core-level spectra at the surface (without etching) of pristine and 10 wt% PFI-doped films are shown in Figure 1c. The S(2p) peaks observed at 169 eV correspond to the sulfur signal from sulfonate, while the two peaks at 163.48 and 164.48 eV correspond to the sulfur signal from S-P3MEET thiophene[41].

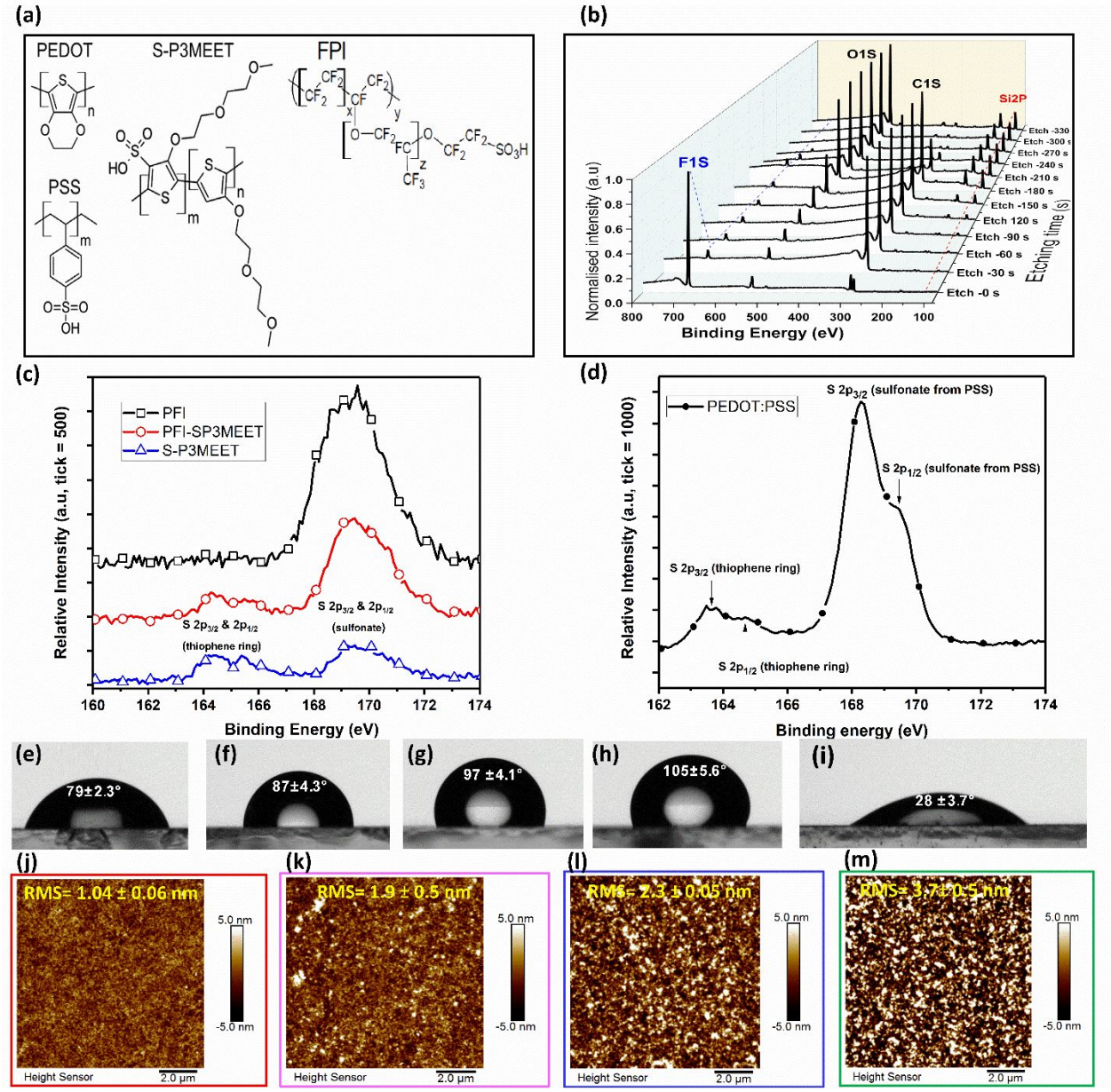

Figure 1. (a) Schematic diagram of the structure of PEDOT:PSS, S-P3MEET, and PFI. (b) XPS depth profiling of the S-P3MEET-PFI-10% wt film with etching times of 0-330 s. (c) XPS of S(2p) core-level spectra at the surface for: pristine and 10 wt% PFI-doped S-P3MEET, and PFI (d) PEDOT:PSS. Water drop contact angles of: (e) pristine S-

P3MEET, (f) S-P3MEET- 5% wt PFI, (g) S-P3MEET- 10% wt PFI, (h) S-P3MEET- 15% wt PFI, and (i) PEDOT:PSS films. AFM morphology of: (j) pristine S-P3MEET, (k) S-P3MEET- 5% wt PFI, (l) S-P3MEET- 10% wt PFI, and (m) S-P3MEET- 15% wt PFI.

After S-P3MEET-PFI blending, the S(2p) core level at 169 eV increased due to the contribution of sulfur n PFI molecules by withdrawing an electron from the conjugated backbone[41], while the intensity of the two peaks of the S(2p) core level of the thiophene remained the same. The sulfonate contribution of the PFI molecules was only on the S-P3MEET surface and disappeared after 30 seconds of etching, indicating less PFI in the bulk than on the surface (Figure S1a). The S(2p) peaks of PEDOT:PSS showed higher intensity than both pristine and fluorinated S-P3MEET, as can be seen in Figure 1d. The two C(1s) peaks on the fluorinated S-P3MEET film surface at a binding energy of 285 eV are attributed to the S-P3MEET, while the peak at 292 eV is attributed to the C−F2 bond of PFI. The C(1s) peak at 292 eV decreased with depth profiling due to the self-segregation of PFI on the film surface (Figure 1b and S1b), which is further evidence of S-P3MEET fluorination. The XPS survey scan of the pristine S-P3MEET, PFI, fluorinated S-P3MEET, and PEDOT:PSS samples can be found in Figure S1c.

The organization of PFI on the S-P3MEET surface was further analyzed by water contact angle (WCA) analysis. The WCAs of the HTLs (on an indium tin oxide (ITO) glass substrate) are shown in Figure 1e-i and Figure S2. The average WCA of S-P3MEET was 79±2.3° (Figure 1e); the contact angle gradually increased as the PFI ratio in the polymer increased, from 87±4.3° to 97±4.1° to 105±5.6° with 5% wt, 10% wt, and 15% wt PFI, respectively (Figure 1f-h). The WCA of PEDOT:PSS was 28±3.7°, lower than that of the pristine S-P3MEET. This result confirms that the surface of pristine S-P3MEET is more hydrophobic than the PEDOT:PSS film. A hydrophobic capping layer on the surface of the HTLs provided resistance to moisture and environmental conditions, benefiting the perovskite upper layer. The impact of PFI doping ratio on the morphology of the S-P3MEET was investigated using atomic force microscopy (AFM), with scan size of 10 μm x 10 μm. The pristine S-P3MEET layer had a smooth surface with average root mean square (RMS) roughness of 1.04±0.06 nm, compared to the PEDOT:PSS, which exhibited 1.2±0.08 nm RMS roughness (Figure 1j and Figure S3a, respectively). After incorporating PFI in the S-P3MEET, the RMS roughness of this layer increased dramatically, reaching 1.9±0.5 nm for 5%wt PFI then 2.3±0.05 nm for 10 %wt PFI (Figure 1k-l). At the higher doping level of 15%wt PFI, the RMS roughness of the S-P3MEET surface further increased to 3.7±0.3 nm (Figure 1m).

The AFM height images (Figure 1m) clearly indicate that the morphology of the PFI-doped S-P3MEET surface was influenced by the PFI. The hydrophobic fluorocarbon backbone and hydrophilic sulfonic acid groups, which preferentially interact with thiophene rings, likely led to the formation of grains that aggregated as bright regions on the surface[30,36]. The bright aggregated grains increased as the PFI doping level increased in the polymer, whereas the PFI film itself had a highly smooth surface, with less than 0.7 nm RMS roughness (Figure S3b). These variations in RMS after incorporation of PFI influence the optoelectronic properties of the fluorinated S-P3MEET films.

Scanning electron microscopy (SEM) top-view images of the triple-cation lead mixed-halide $Cs_{0.04}(FA_{0.83}MA_{0.17})_{0.95}Pb(I_{0.83}Br_{0.17})_3$ films are shown in Figure 2a-e. Using solution process, the perovskite films were prepared by spin-coating the perovskite solution onto the pristine S-P3MEET and fluorinated S-P3MEET substrate. In this process, mixed $HC(NH_2)_2I$ (FAI) and CH_3NH_3Br (MABr) in isopropyl alcohol with 4 mg/ml concentration was dropped onto the spinning substrate to enhance the Ostwald ripening of secondary grain growth of the perovskite films[44–48]. In this process, according to Fick's first law, the high gradient concentration will cause faster mass transportation between small grains (in treatment solution) and large grains (from precursor solution that is beginning film formation)[44]. As a result, enough small grains in solution are re-deposited onto the large grains (de-nucleation of the larger grain) to enable the nucleation process to continue during spin-coating, leading to larger grain sizes[45–48]. More details about the $Cs_{0.04}(FA_{0.83}MA_{0.17})_{0.95}Pb(I_{0.83}Br_{0.17})_3$ deposition process are given in the Experimental Section.

Compared to the perovskite deposited onto the pristine S-P3MEET, the fluorinated S-P3MEET surface influenced perovskite growth more. Increasing the PFI doping ratio in the polymer led to reduced grain size growth of the perovskite films. This finding is due to the lower wettability of the mixed-cation lead mixed-halide perovskite precursor solution on the fluorinated S-P3MEET substrate[49,50]. Increasing the PFI doping level in the S-P3MEET polymer more led to further reduction in grain size of the perovskite films due to the acidity of the PFI[51,52]. It has been reported that depositing perovskite onto a neutral HTL enhances the nucleation and crystallization of a perovskite active layer, with more uniform grain sizes, than depositing it onto acidic and/or basic HTL surfaces[25,27,37]. To overcome this issue and enhance the wettability of the triple-cation perovskite precursor solution onto the fluorinated S-P3MEET substrate, the blended solution of S-P3MEET and PFI was diluted with a mixture of deionized water (10%) and isopropyl alcohol

(30%). Although the fluorinated S-P3MEET reduced the grain size of triple-cation perovskite active layers, all the processes resulted in pinhole-free perovskite films with dense surface morphologies. Furthermore, organic halide post-treatment caused a novel grain boundary passivation (stitching) effect when the CsFAMA perovskite was deposited onto pure S-P3MEET, which was not seen when the perovskite film was deposited onto the PEDOT:PSS substrate. The lower grain size and lower grain boundary passivation perovskite films on the PEDOT:PSS surface could be attributed to the wettability and control over the Ostwald ripening process[48,49].

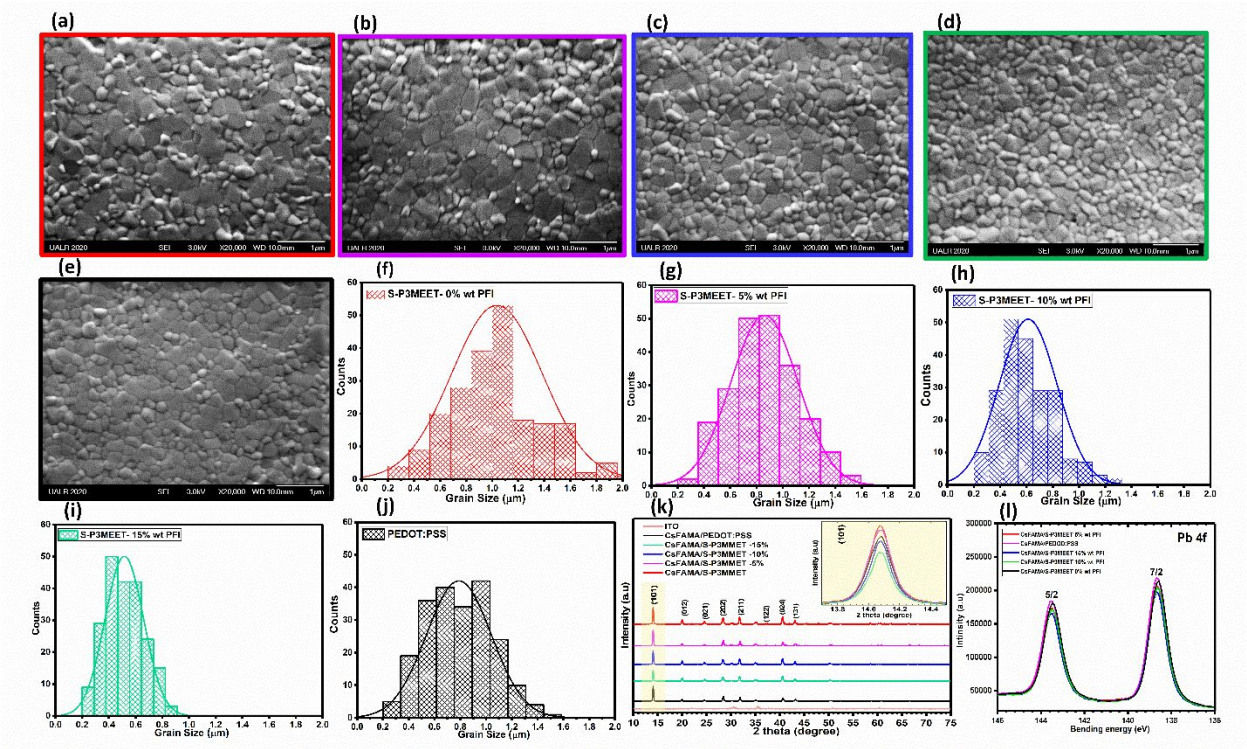

Figure 2. (a-j) Top-view SEM images and grain size statistics of the CsFAMA perovskite film deposited onto: (a & f) pristine S-P3MEET, (b and g) S-P3MEET- 5% wt PFI, (c & h) S-P3MEET- 10% wt PFI, (d & i) S-P3MEET- 15% wt PFI/ITO, and (e & j) PEDOT:PSS. (k) XRD patterns of the perovskite films deposited onto HTLs/ITO substrate, and (l) XPS narrow scan for CsMAFA perovskite films of Pb 4f core level.

The grain size statistics (Figure 2f-j) showed that the average grain sizes of the perovskite films were 1.05 μm, 0.88 μm, 0.62 μm, 0.51 μm, and 0.796 μm when perovskite was deposited onto the pristine S-P3MEET, S-P3MEET- 5% wt PFI, S-P3MEET- 10% wt PFI, S-P3MEET- 15% wt PFI, and PEDOT:PSS, respectively. The reduced perovskite grain size on the S-P3MEET- 15% wt PFI surface suggests that the high acidity began to be dominant due to the high PFI doping level[36]. As can be seen in Figure 2k, the X-ray diffraction (XRD) patterns of CsFAMA deposited

onto HTLs/ITO were identical, indicating the black perovskite phase had been formed[53]. Furthermore, the composition of a $(PbI_{1-x}\ Br_x)_2$ peak was not observed for all the perovskite films. This result indicates that the impurities in the perovskite films were removed successfully when the CsFAMA perovskite was treated with mixed cation and mixed halide in IPA anti-solvent. The magnified images of the main XRD peaks at 14.08° position and 101 planes are shown in the inset of Figure 2k. As can be seen, the $Cs_{0.04}(FA_{0.83}MA_{0.17})_{0.95}Pb(I_{0.83}Br_{0.17})_3$ perovskite films deposited onto pristine S-P3MEET exhibited peaks that were slightly more intense than the other perovskite films. This could be due to perovskite films exhibiting better orientation on the pristine S-P3MEET surface than on the fluorinated S-P3MEET and PEDOT:PSS surfaces. The results of X-ray photoelectron spectroscopy (XPS) survey scans showed that the CsFAMA perovskite components were formed into all the types of HTLs (Figure S4). The narrow scans of Pb 4f core levels for all perovskite films (Figure 2l) show sharp doublet peaks of the Pb $4f_{5/2}$ (143.5 eV) and Pb $4f_{7/2}$ (138.6 eV), which are related to the Pb^{2+} in the perovskite composition (PbI_2, $PbBr_2$)[54]. We did not observe any metallic lead from excessive and/or unsaturated PbI_2 on the film surface. XRD analysis confirmed this observation for all CsFAMA-prepared films.

The stock solutions of the inorganic components (CsI, PbI_2, and $PbBr_2$) were heated at 150^0C, which caused them to dissolve entirely, leading to a clear solution. This heating process lowers excess $(PbI_{1-x}\ Br_x)_2$ accumulation on the perovskite film surface[45], which would otherwise create poorer-quality perovskite active layers and, as a result, reduce PSC performance[55,56]. Additionally, the morphology of $Cs_{0.04}(FA_{0.83}MA_{0.17})_{0.95}Pb(I_{0.83}Br_{0.17})_3$ perovskite films deposited onto different HTLs was analyzed using AFM (Figure S4a-f). Additionally, the morphology and roughness of perovskite films deposited onto different HTLs were analyzed using AFM (Figure S4a-f). The AFM scanning area was 5 μm x 5 μm over randomly chosen spots on the perovskite films' surfaces. The average RMS roughness of the AFM images was 9 ±1 nm , 10 ±1 nm, 12 ±1 nm, 17 ±3, and 12±2 nm for perovskite deposited onto the pristine S-P3MEET, S-P3MEET- 5% wt PFI, S-P3MEET- 10% wt PFI, S-P3MEET- 15% wt PFI, and PEDOT:PSS, respectively.

2.2. Optoelectronic properties

To investigate the impact of PFI doping on surface properties, the contact potential difference or surface potential (CPD) of the HTLs was mapped using Kelvin probe force microscopy (KPFM). The histogram distributions of the CPD for all HTLs are presented in Figure 3a-e. The

average CPD between the conductive tip and the surface of the HTLs was -115±3 mV, - 418±2 mV, - 561±2 mV, - 589±6 mV, and 9±8 mV for pristine S-P3MEET, S-P3MEET- 5% wt PFI, S-P3MEET- 10% wt PFI, S-P3MEET- 15% wt PFI, and PEDOT:PSS, respectively. CPD was negative for all S-P3MEET films because their WF was higher than the tip;[21] the CPD further decreased when the PFI doping ratio increased (Figure 3a-d). It is very interesting to note that local variations in the CPD for all HTLs are relatively nil at four different spots on the same sample, as can be seen in KPFM mapping images (Figures S6 and S7). On the other hand, high variations in CPD values were observed based on the PFI doping ratio in S-P3MEET films because of the fluorinated capping layer at the polymer interface. The absolute surface WF can be estimated after the tip is calibrated with a highly oriented pyrolytic graphite (HOPG) sample[49]. As labeled in Figure 3f, the average WF increased as the content of PFI increased in the S-P3MEET polymer. Eventually, a composition of S-P3MEET-PFI with a very high WF was created, featuring easily tuned values from -4.98 eV to -5.45 eV when the PFI content was increased from 0% wt to 15% wt, respectively. The WFs of the fluorinated and pristine S-P3MEET polymers were much deeper than the WF obtained by the PEDOT:PSS film due to the lower CPDs of the pristine and fluorinated S-P3MEET polymers. This finding is crucial for improving the alignment energy and minimizing potential energy loss at perovskite/HTL interfaces, which is important for enhancing the performance of PSCs[19,20]. The WFs of the fluorinated and pristine S-P3MEET estimated by KPFM in this work are consistent with Mauger et al.'s,[41] which were measured with a different technique. Furthermore, the WF of the PEDOT:PSS film measured in this work was approximately in agreement with the ultraviolet photoelectron spectroscopy results reported by Lim et al.[35].

To investigate the impact of PFI doping on the optical properties of S-P3MEET, the UV-Vis spectroscopic spectra for transmittance and reflection were recorded for doped and undoped S-P3MEET films deposited onto an ITO/glass substrate as well as PFI/ITO glass (Figure 3(g-h)). The PFI-doped S-P3MEET films showed enhanced transmittance in the wavelength range from 460 nm toward infrared region compared to the undoped S-P3MEET film. Compared with PFI/ITO alone, the PFI-doped S-P3MEET also showed enhanced transmittance in the interval wavelength range of 500−660 nm, where the transmittance increased as PFI doping increased. The transmittance spectra of the pristine S-P3MEET showed higher transmittance than PEDOT:PSS from 600 nm toward the infrared region; inversely, transmittance was reduced toward the UV region. On the other hand, the pristine S-P3MEET film showed high absorption peak at 375−600

nm and low absorption peaks at longer wavelengths after 600 nm due to the π–π* transitions and the "free carrier tail"[57].

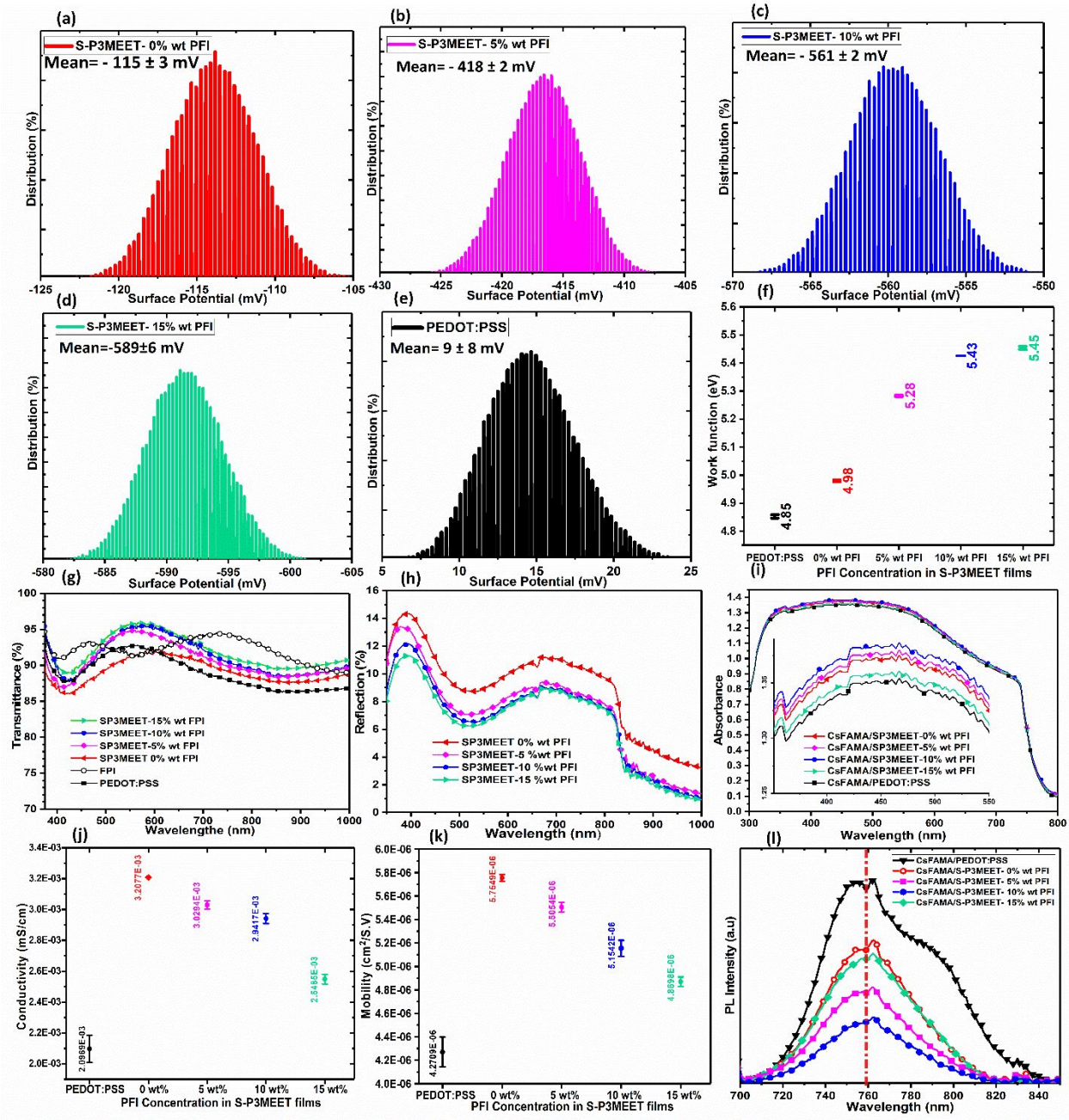

Figure 3. (a-e) Distribution histograms of the surface potential of HTLs. (f) Work function estimation. (g) UV-Vis transmittance spectra of HTL. (h) UV-Vis reflection spectra of HTL. (i) UV-Vis absorption spectra of perovskite, inset shows zoomed in region from 350-550nm for clarity. (j) Conductivity and (k) mobility for pristine S-P3MEET. PFI-doped S-P3MEET and PEDOT:PSS as (HTL) films deposited onto ITO/glass substrates. (l) Steady-state PL spectra of CsFAMA perovskite layer deposited onto HTLs /quarters substrate.

The reflection spectra of doped and undoped S-P3MEET films deposited onto ITO/glass substrates were further studied. It can be concluded from Figure 3h that the reflection spectra of S-P3MEET decreases when the PFI doping ratio increases. Reducing the reflection spectra from the S-P3MEET-doped surface is another benefit that can increase light harvesting by the perovskite active layer. The capping layer of rich doping PFI onto the S-P3MEET surface can act as an antireflection layer as in previous reports, which increases the photocurrent generated by the perovskite[29,36]. Even though the transmittance and reflection characteristics are steadily improved when increasing the doping level up to 15%wt PFI, it also can come at a cost by negatively influencing the wettability of the perovskite over higher PFI doping levels of SP3MEET. This in turn can result in poor perovskite film quality leading to poor absorption characteristics and hence device performance. To examine any differences in the light harvesting characteristics of the $Cs_{0.04}(FA_{0.83}MA_{0.17})_{0.95}Pb(I_{0.83}Br_{0.17})_3$ perovskite deposited onto the different HTL films, their UV-Vis absorption spectra were compared (Figure 3i), and no significant differences were seen at the full scale. However, when zooming into to more closely examine the data (see inset of Figure 3i), it is clear that the perovskites deposited on 5% and 10% PFI-doped films exhibit higher absorption through the visible region (the inset data was cut at 550nm to fit in the area more easily). This is also manifest in the quantum efficiency data present later (Figure 5f), where devices based on the 5% and 10% PFI-doped SP3MEET exhibit improved characteristics. The optical band gap (E_g) of $Cs_{0.04}(FA_{0.83}MA_{0.17})_{0.95}Pb(I_{0.83}Br_{0.17})_3$ perovskite deposited onto pristine and fluorinated S-P3MEET and PEDOT:PSS was calculated similarly to our previous report[49]. The estimated E_g of the perovskite prepared via a (FAI+MABr)/IPA treatment process was 1.63 eV. Even though the Eg of the perovskite active layer can be affected by different sizes of particles or crystallization of the perovskite structures[58], the estimated E_g of the perovskites was approximately the same for all the preparations (Figure S9).

Furthermore, the PSCs' conductivity and mobility were investigated using I-V curves and a space charge limited model (SCLC) to determine the effect of PFI on the electrical properties of the S-P3MEET polymer (Figure S10a and b). The average conductivity and mobility values are depicted in Figure 3j and Figure 3k, respectively. As can be seen, the pristine S-P3MEET polymer has high conductivity—3.21×10^{-3} mS/cm—compared to PEDOT:PSS—2.1×10^{-3} mS/cm—at the same thickness. It was found that the conductivity and mobility of fluorinated S-P3MEET were

reduced when the PFI doping ratio increased in the polymer. As confirmed by AFM results, the separation of S-P3MEET agglomerates by PFI doping led to reduced conductivity for the doped S-P3MEET[31]. The conductivity of the fluorinated S-P3MEET is consistent with previous literature,[31,41] and the characterization of its optoelectronic and morphological properties indicates its usefulness in inverted perovskite devices.

To further investigate the HTL/perovskite interface, the steady-state photoluminescence (PL) of the CsFAMA perovskite films deposited onto pristine and fluorinated HTLs was used to evaluate the nonradiative recombination characteristics. The perovskite deposited onto S-P3MEET- 10% wt PFI exhibited a lower PL intensity than the other perovskite films, indicating the HTL's excellent ability to facilitate the extraction of photogenerated holes at the HTL/perovskite interfaces due to the better energy alignment level of this formulation. Conversely, with other HTLs such as pure S-P3MEET and/or PEDOT:PSS, the photogenerated holes were more confined in the perovskite layer due to the interfacial energy barrier, leading to high PL intensity[59–61]. All the PL peak positions for the CsFAMA perovskite films were consistent at 759.5 nm, without a change in the emission peak position (Figure 3L).

2.3. Evaluation of photovoltaic performance

In this study, inverted planar PSCs with a structure of ITO/HTL/$Cs_{0.04}$ $(MA_{0.17}FA_{0.83})_{.96}$ $Pb(I_{0.83}Br_{0.17})_3$/phenyl-C_{61}-butyric acid methyl ester (PCBM)/bathocuproine (BCP)/silver (Ag) were fabricated to optimize the HTLs and perovskite active layer.

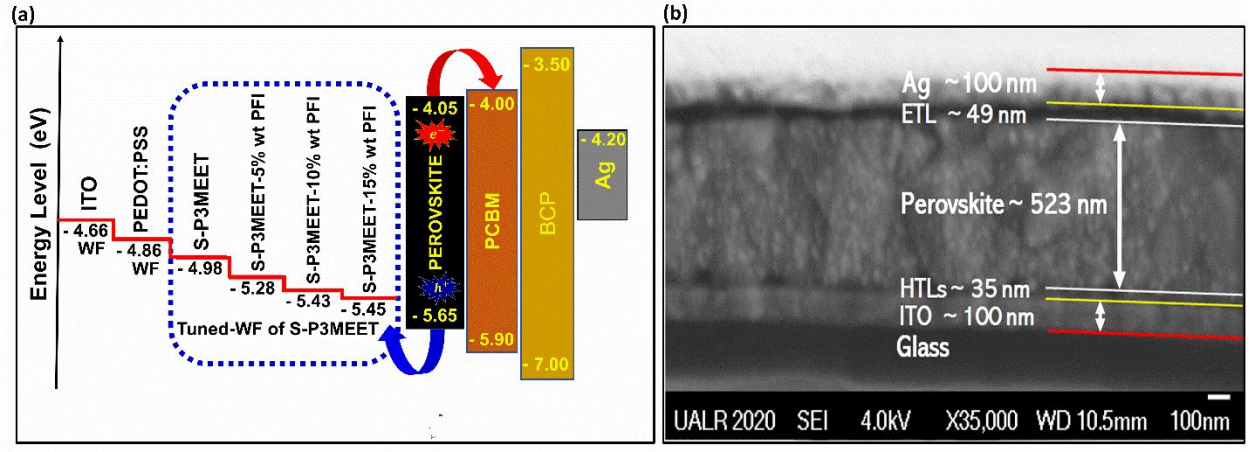

Figure 4. (a) Energy level and work function diagram of the PSC devices and (b) cross-section of SEM image showing the PSC configuration and thickness information for the whole PSC device. Here, the energy levels of the electrodes and electron transport layers are taken from references. 49 and 62, while the energy level of perovskite is taken from reference 63.

The energy level diagram of the inverted planar configuration is presented in Figure 4a. The energy level of electron transport layers and electrodes is taken from previous work[49,62], while the energy of triple-cation perovskite valence-band maximum (VBM) and conduction-band maximum (CBM) are taken from Gelmetti et al[63]. To grow the CsFAMA perovskites with large grains and novel passivation grain boundary onto the fluorinated S-P3MEET, saturated anti-solvent with organic halide was important for enhanced Ostwald Ripening[45,64]. All the HTL films' thickness was optimized to be 35 ±1 nm, as estimated via AFM in tapping mode (Figure S8). SEM cross-section characterization further confirmed the HTL thickness (Figure 4b). The thickness information for the fabricated inverted planar PSC was as follows: ITO: 100 nm, HTLs: ~35 nm, perovskite: ~523 nm, ETLs (PCBM/BCP): ~ 49 nm, Ag: 100 nm. It has been found that the performance of a PSC device is influenced by the thickness of the active layer[65,66]; therefore, the perovskite thickness was optimized in this work to be ~523 nm, which is considered ideal for triple-cation perovskite in the inverted planar architecture[66–68].

To investigate the effect of doping S-P3MEET with PFI on the device's photovoltaic performance and to compare the results of pristine S-P3MEET with a control device based on a PEDOT:PSS HTL, five groups of PSC devices were made, and all devices, except for the HTL components, were fabricated under the same conditions. Figure 5a-e shows current density-voltage (J−V) curves of the PSC devices, measured at room temperature (RT). For all PSCs, the photovoltaic parameters were separately evaluated in both forward scan (Fs) and reverse scan (Rs) directions, and the results from the best, or "champion," devices are summarized in Table 1. As can be seen in Figure 5a-e and Figure S11, the Voc increased remarkably when PFI doping level increased in the S-P3MEET. The increase in Voc from 0.965 V (pristine S-P3MEET) to 1.070 V for S-P3MEET-10% wt PFI results from the higher work function of the fluorinated S-P3MEET polymer[38]. This finding is caused by the minimized potential energy loss at the perovskite/HTL interfaces, resulting from the good energy alignment of triple-cation perovskite with a VBM of -5.65 eV[69] with the WF of the fluorinated S-P3MEET (5.28−5.45 eV). The enhancement of Voc due to modifying the work function of the HTLs was previously reported in the inverted planar

PSC structure[35,65,70]. It was noted that the FF of the PSC devices decreased with PFI doping level in the S-P3MEET polymer, from 80% to 72% at 15% wt PFI doping ratio. This finding is attributed to the increased series resistance (R_s) and/or poor shunt resistance (R_{sh}) of the contact HTL[28,48,50].

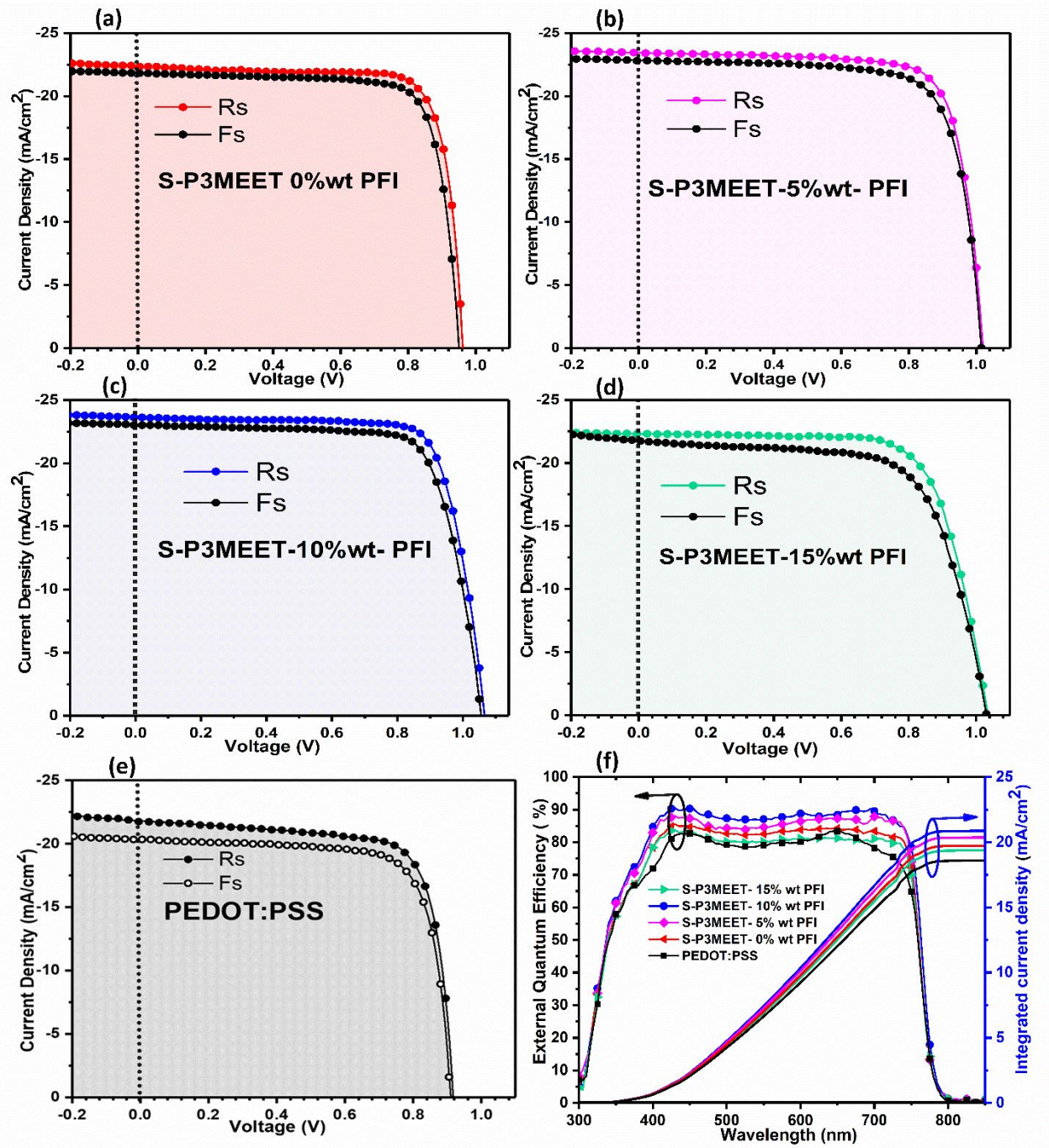

Figure 5. (a-e) J-V characteristics of forward scan (FS) and reverse scan (RS) measurements under standard AM 1.5 Illumination (100 mW /cm^2) of the champion PSCs with different HTLs: (a) pristine S-P3MEET, (b) S-P3MEET- 5% wt PFI, (c) S-P3MEET- 10% wt PFI, and (d) S-P3MEET- 15% wt PFI, as well as (e) the control PSC, PEDOT:PSS.

(f) EQE spectra and integrated current density calculation from EQE of the PSC based on pristine S-P3MEET, fluorinated S-P3MEET, and PEDOT:PSS control device.

However, we believe that reducing the grain size growth of the perovskite on the high-acidity fluorinated S-P3MEET HTL was the main reason for dropping the FF of the PSC device. In addition to the increased Voc of the fluorinated S-P3MEET-based device, the J_{SC} also increased from 22.35mA/cm^2 (pristine S-P3MEET) to 23.61 mA/cm^2 (S-P3MEET- 10% wt PFI).

Table 1. Performance data for the champion PSCs with different HTLs; the average values were obtained for 42 devices, measured at Rs for each type of device.

HTL Material	Scan direction	J_{sc} mA.cm^{-2} from		V_{oc} (V)	FF (%)	PCE (%)	HI	R_{sh} (Ω .cm^2)	R_s (Ω .cm^2)
		EQE	J-V						
S-P3MEET- 0% wt PFI	Forward	19.77	21.80	0.950	80	16.46	0.0219	1384	42
	Reverse		22.35	0.965	80	17.25			
	Average		22.2 ±0.51	0.952 ±0.023	78.2 ±3	16.31 ±0.822			
S-P3MEET- 5% wt PFI	Forward	20.46	22.90	1.015	76	17.66	0.0251	1264	63
	Reverse		23.30	1.020	78	18.42			
	Average		22.4 ±0.65	0.973 ±0.025	75.31 ±2.41	16.43 ±0.820			
S-P3MEET- 10% wt PFI	Forward	21.09	22.90	1.060	76	18.44	0.0253	1298	53
	Reverse		23.61	1.070	78	19.60			
	Average		23.02 ±0.66	1.03 ±0.025	75.57 ±2.51	17.74 ±1.12			
S-P3MEET- 15% wt PFI	Forward	19.47	21.71	1.03	69	15.44	0.0495	553	108
	Reverse		22.20	1.04	72	16.55			
	Average		21.68 ±0.89	1.02 ±0.023	68.33 ±3.8	15.08 ±1.05			
PEDOT:PSS (control device)	Forward	18.68	20.18	0.910	76	13.95	0.0600	903	121
	Reverse		21.35	0.920	76	14.97			
	Average		20.75 ±1.33	0.885 ±0.024	76.52 ±4	14.01 ±1.35			

Even though the perovskite based on S-P3MEET- 5% wt PFI and/or S-P3MEET- 10% wt PFI showed lower grain size and crystallographic features, the enhancement of the Jsc may result from higher charge carrier transport at the perovskite/HTLs interface[35,70–72], as indicated by the steady-state PL characterization. Furthermore, the capping layer of rich PFI onto the S-P3MEET surface acts as an antireflection layer, enhancing the light harvesting and the photogenerated current.

For reverse scan (Rs) measurements, the pure S-P3MEET perovskite device exhibited a power conversion efficiency (PCE) of 17.25% with a V_{OC} of 0.965 V, a J_{SC} of 22.35 mA/cm^2, and an FF of 80%. When a 5% wt PFI doping ratio was added, the PCE increased remarkably to 18.24% with a V_{OC} of 1.020 V, a J_{SC} of 23.30 mA/cm^2, and an FF of 78%. The best-performing S-P3MEET

device (19.6% PCE) was obtained using an HTL with 10% wt PFI doping ratio; this device also exhibited the following Rs measurements: V_{OC} of 1.070 V, FF of 78%, and J_{SC} of 23.60. Increasing the PFI doping ratio to 15% wt led to poor performance (PCE of 15.37% due to drops in both the FF and J_{SC}). In order to compare the results of these alternative S-P3MEET HTLs, a control device was fabricated based on PEDOT:PSS, which is often used in the inverted planar structure. In reverse scan, the Voc, Jsc, and FF of the PEDOT:PSS-based device were 0.920 V, 21.35 mA/cm^2, and 76%, respectively, resulting in a PCE of 14.97% (Figure 5e). This reduced performance is attributed to the poor energy alignment at the perovskite/HTL interface, which reduced the V_{OC} due to the lower WF of PEDOT:PSS. Furthermore, according to the literature, the organic cation of perovskite components can decrease the intrinsic p-doping in PEDOT:PSS, resulting in further reduction of the WF and non-efficient hole collection[38,73]. The hysteresis degrees of the inverted PSCs with different HTLs and CsFAMA perovskite preparation with (FAI+MABr)/IPA treatment were also evaluated using hysteresis index (HI) formula [74].

As can be seen in Table 1, the HI of the PSC devices based on pristine S-P3MEET, S-P3MEET- 5% wt PFI, S-P3MEET- 10% wt PFI, S-P3MEET- 15% wt PFI, and PEDOT:PSS HTLs are 0.0219, 0.0273, 0.0251, 0.0389, and 0.0600, respectively. According to the literature, hysteresis depends largely on carrier transport contact materials, crystal size, and ion migration of the perovskite active layer[35,70,71,75]. While variations in the degree of hysteresis were seen in the different HTLs, we believe that the high quality of the perovskite film preparation with (MABr+FAI)/IPA treatment is the main reason for the reduced hysteresis in the all of the PSCs.

The external quantum efficiency (EQE) spectra and integrated J_{SC} response of the PSC devices with different HTLs are presented in Figure 5f in the wavelength range 300-850 nm. The Jsc for PSC devices were further confirmed by EQE test, as listed in Table 1. The small variation between the Jsc obtained from the J−V curves and the EQE test is attributed to the different setup for the J-V curves and the EQE. In the EQE measurement, the device is illuminated by a smaller spot-size (~1mmx1mm) within the device area compared to the aperture masked area (1.6mm x 1.6mm) in J-V measurement. This likely results in the slight differences in the Jsc from EQE versus measurement in the J -V curve. The EQE values of S-P3MEET-based PSC devices with 10 wt% and 5 wt% PFI doping demonstrate an increase in response over the entire wavelength range. This is consistent with the decreased reflection and increased transmittance of HTL over the same wavelength range, in addition to the increased absorption of the perovskite. Therefore, the Jsc

enhancement can be partially attributed to improvement in the light harvesting in addition to the energy level alignment of the PFI doped films.

To study the statistical distribution of the PSC devices and check their experimental reproducibility, we fabricated 42 devices based on each type of HTL and control device based on PEDOT:PSS. Figure 6 shows the statistical distribution for the key parameters of the PSC devices: Voc, J_{SC}, FF, and PCE.

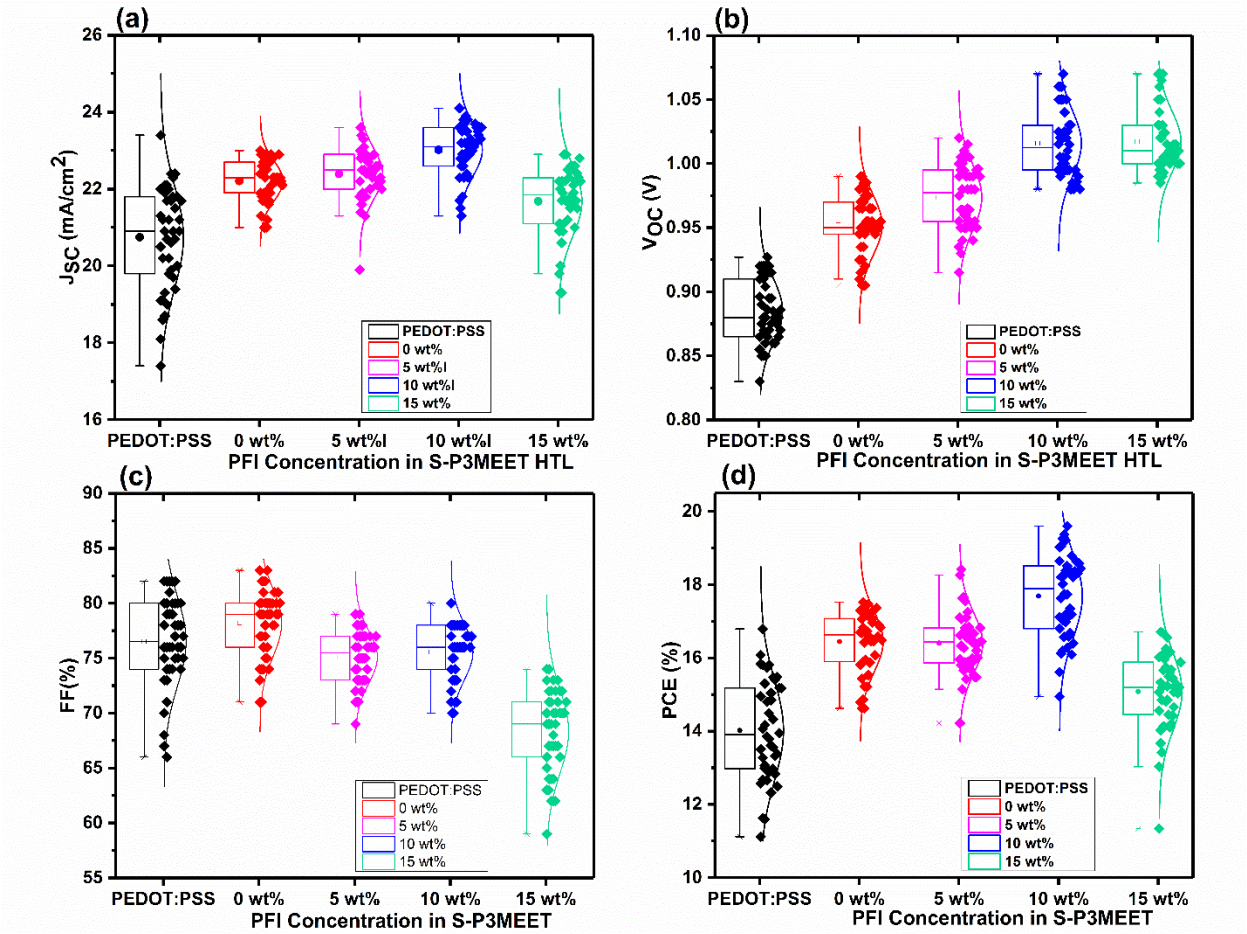

Figure 6. Statistical distribution of the (a) Jsc, (b) Voc, (c) FF, and (d) PCE of 5 different types of devices (42 PSC devices tested total). Data shown are the mean values (solid circle), median line (line in the box), the standard deviation of the data distribution (box), and the upper and lower accepted data limits (whiskers; a coefficient of 1.5 was used)—any point outside of this was considered an outlier.

This statistical study shows that the PSCs based on typical HTLs displayed trends similar to the J–V results of the champion devices (Figure 5). This suggests that the devices have excellent reproducibility with minimal cell parameter fluctuations. For reverse scan direction, the average PCE of the devices based on pristine S-P3MEET, S-P3MEET- 5% wt PFI, S-P3MEET- 10% wt

PFI, S-P3MEET- 15% wt PFI, and PEDOT:PSS HTLs were 16.31±0.82%, 16.43±1.12%, 17.74±1.12%, 15.08±1.05%, and 14.01±1.35%, respectively. Consistent with the above analysis, PSC devices with S-P3MEET- 10% wt PFI HTLs exhibited the best PCE. The PSC improvements seen with the S-P3MEET- 10% wt PFI HTLs are attributed to the WF of the HTLs, which had good energy alignment at the perovskite interface, leading to enhanced device V_{OC}. In addition to the modified HTLs, preparing perovskite films with mixed organic halide (FAI+MABr)/IPA treatment also enhanced the quality of the perovskite layer. A high-quality perovskite active layer with enlarged grain size and uniform surfaces is crucial for inhibiting carrier recombination and enhancing the performance of the PSC. Even though the HTLs based on S-P3MEET- 15% wt PFI showed higher WF, the overall low quality (high roughness/low grain size) of the perovskite films leads to increased defects and recombination sites ultimately resulting in a drop in PSC performance. Moreover, the conductivity of the SP3MEET-15% PFI HTL was also lower than other SP3MEET HTLs (Figure 3j) thereby increasing the series resistance and leading to decreased FF and efficiency.

Long-term stability is another important factor in determining PSC performance. To examine the impact of HTLs on device stability, the non-encapsulated PSC devices based on different HTLs, including pristine S-P3MEET, fluorinated S-P3MEET, and PEDOT:PSS, were stored under ambient conditions of relative humidity (RH) (50-75%) in the dark.

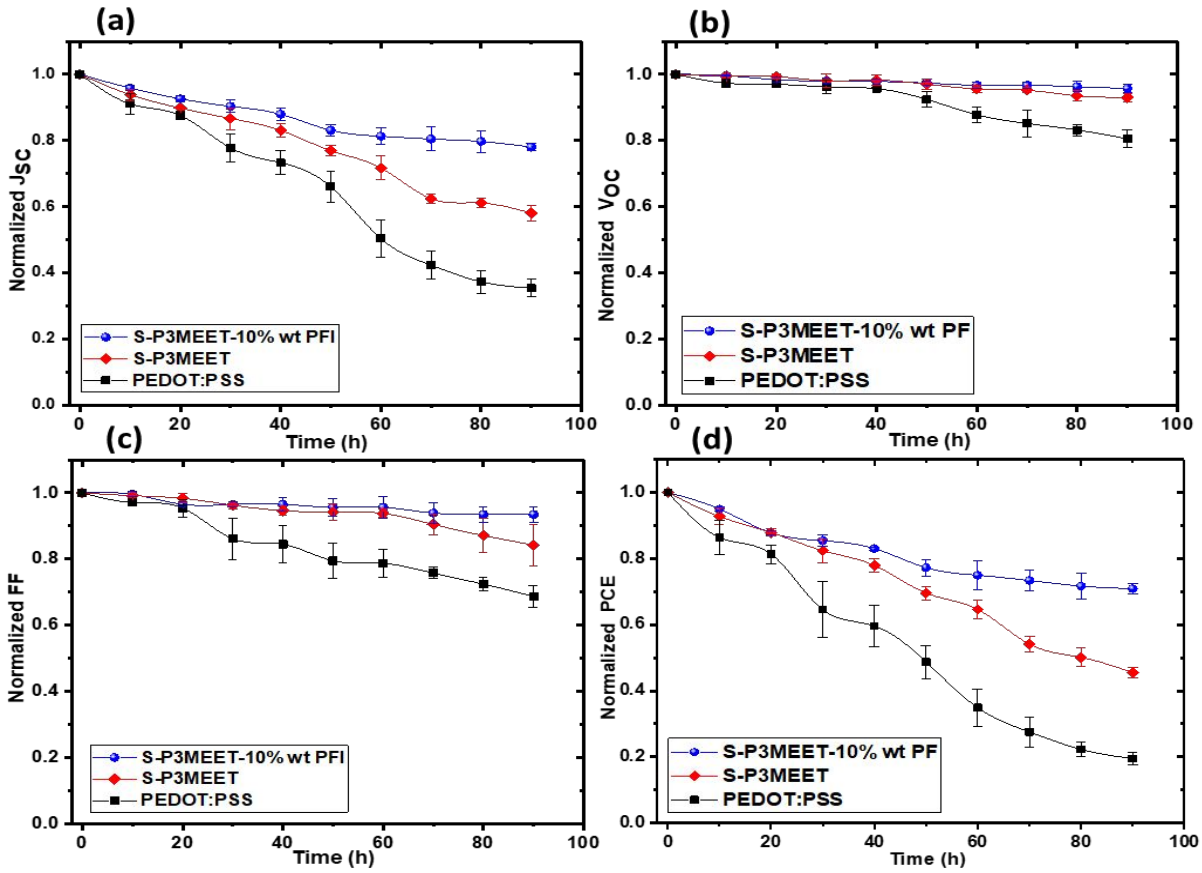

Figure 7. Normalized (a) JSC, (b) VOC, (c) FF, and (d) PCE of unencapsulated PSCs based on pristine S-P3MEET, fluorinated S-P3MEET, and PEDOT:PSS HTLs stored in the dark and under ambient conditions with a range of relative humidity (50-70%) at 25°C.

The PSC stability test results were averaged from 3 different devices, and the solar cell parameters were normalized to the initial values obtained after device preparation. As shown in Figure 7, the PSC based on fluorinated S-P3MEET exhibited superior stability, as indicated by 73% retention of the initial PCE versus 50% PCE retention by the device with pristine S-P3MEET after 80 h; in contrast, the PEDOT:PSS-based devices only maintained 22% of their initial PCEs. As can be seen, the main loss of PCE was attributed to the J_{SC} and FF, which could be due to increased trap density[76]. As we discussed, the control device's weaker stability is caused by PEDOT:PSS's hygroscopic nature, which influences the moisture-sensitive perovskite films. The hydrophobic nature of the HTL films (SP3MEET + PFI) studied here prevents diffusion of moisture to the active layer (perovskite) and enhances device stability.

3. Conclusions

In this study, we demonstrated an effective method to enhance the efficiency and stability of triple-cation perovskite in inverted planar architecture by incorporating hydrophobic PFI into S-P3MEET HTLs. The fluorinated S-P3MEET films showed improved light transmittance, leading to better light harvesting by the perovskite active layer. Furthermore, the WF of the S-P3MEET films was relatively easily tuned after PFI doping, from 4.98 eV to 5.45 eV. PSC devices based on fluorinated S-P3MEET HTLs showed an increase in both J_{SC} and V_{OC} due to the better energy level alignment at the perovskite/HTL interfaces. Compared with the pristine and/or fluorinated S-P3MEET films, the conventional PEDOT:PSS film exhibited lower conductivity, mobility, and WF, leading to lower performance. Most importantly, the stability of PSCs based on fluorinated S-P3MEET HTLs improved due to the PFI giving the film surface high hydrophobicity and chemical stability. We believe that the hydrophobicity of the capping layer of rich doping PFI on the surface of the S-P3MEET polymer protects the upper perovskite layer, further improving the stability of the PSC devices compared to other HTLs.

Conflicts of interest

There are no conflicts to declare.

Acknowledgements

We acknowledge partial support from the Center for Advanced Surface Engineering, under the National Science Foundation Grant No. OIA-1457888 and the Arkansas EPSCoR Program, ASSET III. We also acknowledge partial support from the National Science Foundation (award number 1003970) and the Arkansas EPSCoR Program, ASSET II. We also acknowledge the editorial support of Emily Davis. We also would like to thank Sam Macchi from the laboratory of Dr. Noureen Siraj in the Chemistry Department at UA Little Rock for the use of their photoluminescence spectrophotometer.

ASSOCIATED CONTENT

Supporting Information

Additional information, including the experimental details and perovskite solar cell device characterization, is included in the Supporting Information section. Other data in the Supporting Information section include XPS, SEM, and AFM morphology of perovskite and HTLs; energy bandgap of the perovskite; the J−V curves of the PSC based on PEDOT:PSS; characterization of pristine and fluorinated S-P3MEET as new alternative HTLs; representative I–V curves of conductivity; SCLC curves of mobility; the images of CPD maps with height; and AFM thickness measurements of the HTLs.

References.

1 N. Droseros, D. Tsokkou and N. Banerji, *Adv. Energy Mater.*, 2020, **10**, 1–17.

2 J. Cao and F. Yan, *Energy Environ. Sci.*, 2021, **14**, 1286-1325.

3 C. Chen, S. Zheng and H. Song, *Chem. Soc. Rev.,* 2021, **50**, 7250-7329.

4 G. A. Al-Dainy, S. E. Bourdo, V. Saini, B. C. Berry and A. S. Biris, *Energy Technol.*, 2017, **5**, 373–401.

5 A. Mathur, H. Fan and V. Maheshwari, *Mater. Adv.*, 2021, **2**, 5274–5299.

6 Y. Shao, Z. Xiao, C. Bi, Y. Yuan and J. Huang, *Nat. Commun.*, 2014, **5**, 1–7.

7 H. Zhou, C. Qi, L. Gang, L. Song, S. Tze-bing, D. Hsin-Sheng, H. Ziruo, J. You, L. Yongsheng and Y. Yan, *Science (80-.).*, 2014, **345**, 542–546.

8 A. Fakharuddin, M. Seybold, A. Agresti, S. Pescetelli, F. Matteocci, M. I. Haider, S. T. Birkhold, H. Hu, R. Giridharagopal, M. Sultan, I. Mora-Seró, A. Di Carlo and L. Schmidt-Mende, *ACS Appl. Mater. Interfaces*, 2018, **10**, 42542–42551.

9 J. J. Yoo, S. Wieghold, M. C. Sponseller, M. R. Chua, S. N. Bertram, N. T. P. Hartono, J. S. Tresback, E. C. Hansen, J. P. Correa-Baena, V. Bulović, T. Buonassisi, S. S. Shin and M. G. Bawendi, *Energy Environ. Sci.*, 2019, **12**, 2192–2199.

10 Q. Jiang, L. Zhang, H. Wang, X. Yang, J. Meng, H. Liu, Z. Yin, J. Wu, X. Zhang and J. You, *Nat. Energy*, , DOI:10.1038/nenergy.2016.177.

11 M. Park, J. Y. Kim, H. J. Son, C. H. Lee, S. S. Jang and M. J. Ko, *Nano Energy*, 2016, **26**, 208–215.

12 Q. Jiang, X. Zhang and J. You, *Small*, 2018, **14**, 1–14.

13 X. Ren, D. Yang, Z. Yang, J. Feng, X. Zhu, J. Niu, Y. Liu, W. Zhao and S. F. Liu, *ACS Appl. Mater. Interfaces*, 2017, **9**, 2421–2429.

14 A. Dubey, N. Adhikari, S. Venkatesan, S. Gu, D. Khatiwada, Q. Wang, L. Mohammad, M. Kumar and Q. Qiao, *Sol. Energy Mater. Sol. Cells*, 2016, **145**, 193–199.

15 L. Meng, J. You, T. F. Guo and Y. Yang, *Acc. Chem. Res.*, 2016, **49**, 155–165.

16 X. Liu, Y. Cheng, C. Liu, T. Zhang, N. Zhang, S. Zhang, J. Chen, Q. Xu, J. Ouyang and H. Gong, *Energy Environ. Sci.*, 2019, **12**, 1622–1633.

17 K. Rakstys, C. Igci and M. K. Nazeeruddin, *Chem. Sci.*, 2019, **10**, 6748–6769.

18 Q. Lin, A. Armin, P. L. Burn and P. Meredith, *Acc. Chem. Res.*, 2016, **49**, 545–553.

19 Y. Hou, W. Chen, D. Baran, T. Stubhan, N. A. Luechinger, B. Hartmeier, M. Richter, J. Min, S. Chen, C. O. R. Quiroz, N. Li, H. Zhang, T. Heumueller, G. J. Matt, A. Osvet, K. Forberich, Z. G. Zhang, Y. Li, B. Winter, P. Schweizer, E. Spiecker and C. J. Brabec, *Adv. Mater.*, 2016, **28**, 5112–5120.

20 K. Jiang, F. Wu, G. Zhang, P. C. Y. Chow, C. Ma, S. Li, K. S. Wong, L. Zhu and H. Yan, *J. Mater. Chem. A*, 2019, **7**, 21662–21667.

21 H. Elbohy, B. Bahrami, S. Mabrouk, K. M. Reza, A. Gurung, R. Pathak, M. Liang, Q. Qiao and K. Zhu, *Adv. Funct. Mater.*, 2019, **29**, 1–9.

22 S. S. Mali and C. K. Hong, *Nanoscale*, 2016, **8**, 10528–10540.

23 K. G. Lim, S. Ahn, H. Kim, M. R. Choi, D. H. Huh and T. W. Lee, *Adv. Mater. Interfaces*, 2016, **3**, 1–7.

24 H. S. Lin, I. Jeon, R. Xiang, S. Seo, J. W. Lee, C. Li, A. Pal, S. Manzhos, M. S. Goorsky, Y. Yang, S. Maruyama and Y. Matsuo, *ACS Appl. Mater. Interfaces*, 2018, **10**, 39590–39598.

25 B. Vaagensmith, K. M. Reza, M. D. N. Hasan, H. Elbohy, N. Adhikari, A. Dubey, N. Kantack, E. Gaml and Q. Qiao, *ACS Appl. Mater. Interfaces*, 2017, **9**, 35861–35870.

26 S. Mabrouk, B. Bahrami, H. Elbohy, K. M. Reza, A. Gurung, M. Liang, F. Wu, M. Wang,

S. Yang and Q. Qiao, *InfoMat*, 2019, 1–14.

27 Q. Wang, C. C. Chueh, M. Eslamian and A. K. Y. Jen, *ACS Appl. Mater. Interfaces*, 2016, **8**, 32068–32076.

28 Q. Xue, G. Chen, M. Liu, J. Xiao, Z. Chen, Z. Hu, X. F. Jiang, B. Zhang, F. Huang, W. Yang, H. L. Yip and Y. Cao, *Adv. Energy Mater.*, 2016, **6**, 1–9.

29 X. Hou, Q. Li, T. Cheng, L. Yu, F. Wang, J. Lin, S. Dai, Y. Li and Z. Tan, *J. Mater. Chem. A*, 2015, **3**, 18727–18734.

30 S. A. Mauger and A. J. Moulé, *Org. Electron.*, 2011, **12**, 1948–1956.

31 J. Li, I. E. Jacobs, S. Friedrich, P. Stroeve and A. J. Moulé, *Org. Electron.*, 2016, **34**, 172–178.

32 L. A. A. Pettersson, S. Ghosh and O. Inganäs, *Org. Electron.*, 2002, **3**, 143–148.

33 K. Lee, H. Yu, J. W. Lee, J. Oh, S. Bae, S. K. Kim and J. Jang, *J. Mater. Chem. C*, 2018, **6**, 6250–6256.

34 J. C. Yu, J. A. Hong, E. D. Jung, D. Bin Kim, S. M. Baek, S. Lee, S. Cho, S. S. Park, K. J. Choi and M. H. Song, *Sci. Rep.*, 2018, **8**, 3–11.

35 K. G. Lim, H. B. Kim, J. Jeong, H. Kim, J. Y. Kim and T. W. Lee, *Adv. Mater.*, 2014, **26**, 6461–6466.

36 S. Ma, W. Qiao, T. Cheng, B. Zhang, J. Yao, A. Alsaedi, T. Hayat, Y. Ding, Z. Tan and S. Dai, *ACS Appl. Mater. Interfaces*, 2018, **10**, 3902–3911.

37 M. Yi, W. Jang and D. H. Wang, *ACS Sustain. Chem. Eng.*, 2019, **7**, 8245–8254.

38 S. Im, W. Kim, W. Cho, D. Shin, D. H. Chun, R. Rhee, J. K. Kim, Y. Yi, J. H. Park and J. H. Kim, *ACS Appl. Mater. Interfaces*, 2018, **10**, 18964–18973.

39 K. M. Reza, A. Gurung, B. Bahrami, S. Mabrouk, H. Elbohy, R. Pathak, K. Chen, A. H. Chowdhury, M. T. Rahman, S. Letourneau, H. C. Yang, G. Saianand, J. W. Elam, S. B. Darling and Q. Qiao, *J. Energy Chem.*, 2020, **44**, 41–50.

40 S. Feng, Y. Yang, M. Li, J. Wang, Z. Cheng, J. Li, G. Ji, G. Yin, F. Song, Z. Wang, J. Li and X. Gao, *ACS Appl. Mater. Interfaces*, 2016, **8**, 14503–14512.

41 S. A. Mauger, J. Li, Ö. T. Özmen, A. Y. Yang, S. Friedrich, M. D. Rail, L. A. Berben and A. J. Moulé, *J. Mater. Chem. C*, 2014, **2**, 115–123.

42 T. W. Lee, Y. Chung, O. Kwon and J. J. Park, *Adv. Funct. Mater.*, 2007, **17**, 390–396.

43 Y. Xia, K. Sun and J. Ouyang, *Energy Environ. Sci.*, 2012, **5**, 5325–5332.

44 M. Yang, T. Zhang, P. Schulz, Z. Li, G. Li, D. H. Kim, N. Guo, J. J. Berry, K. Zhu and Y. Zhao, *Nat. Commun.*, 2016, **7**, 2–10.

45 G. Al-Dainy, F. Watanabe, A. S. Biris and S. E. Bourdo, *ACS Appl. Energy Mater.*, 2021, **4**, 3297–3309.

46 F. Wang, M. Yang, Y. Zhang, L. Yang, L. Fan, S. Lv, X. Liu, D. Han and J. Yang, *Adv. Sci.*, , DOI:10.1002/advs.201801170.

47 N. D. Pham, V. T. Tiong, D. Yao, W. Martens, A. Guerrero, J. Bisquert and H. Wang, *Nano Energy*, 2017, **41**, 476–487.

48 M. Jung, S. G. Ji, G. Kim and S. Il Seok, *Chem. Soc. Rev.*, 2019, **48**, 2011–2038.

49 G. A. Al-Dainy, F. Watanabe, G. K. Kannarpady, A. Ghosh, B. Berry, A. S. Biris and S. E. Bourdo, *ACS Omega*, 2020, **5**, 1887–1901.

50 X. Lai, M. Du, F. Meng, G. Li, W. Li, A. K. K. Kyaw, Y. Wen, C. Liu, H. Ma, R. Zhang, D. Fan, X. Guo, Y. Wang, H. Ji, K. Wang, X. W. Sun, J. Wang and W. Huang, *Small*, 2019, **15**, 1904715 (1–9).

51 D. Belaineh, R. Q. Png, C. L. McGuiness, M. Mathai, V. Seshadri and P. K. H. Ho, *Chem. Mater.*, 2014, **26**, 4724–4730.

52 J. M. Serpico, S. G. Ehrenberg, J. J. Fontanella, X. Jiao, D. Perahia, K. A. McGrady, E. H. Sanders, G. E. Kellogg and G. E. Wnek, *Macromolecules*, 2002, **35**, 5916–5921.

53 T. Bu, X. Liu, Y. Zhou, J. Yi, X. Huang, L. Luo, J. Xiao, Z. Ku, Y. Peng, F. Huang, Y. B. Cheng and J. Zhong, *Energy Environ. Sci.*, 2017, **10**, 2509–2515.

54 B. Philippe, M. Saliba, J. P. Correa-Baena, U. B. Cappel, S. H. Turren-Cruz, M. Grätzel, A. Hagfeldt and H. Rensmo, *Chem. Mater.*, 2017, **29**, 3589–3596.

55 B. Philippe, T. J. Jacobsson, J. P. Correa-Baena, N. K. Jena, A. Banerjee, S. Chakraborty,

U. B. Cappel, R. Ahuja, A. Hagfeldt, M. Odelius and H. Rensmo, *J. Phys. Chem. C*, 2017, **121**, 26655–26666.

56 J. Yang, Q. Hong, Z. Yuan, R. Xu, X. Guo, S. Xiong, X. Liu, S. Braun, Y. Li, J. Tang, C. Duan, M. Fahlman and Q. Bao, *Adv. Opt. Mater.*, 2018, **6**, 1–8.

57 J. Hossain, Q. Liu, T. Miura, K. Kasahara, D. Harada, R. Ishikawa, K. Ueno and H. Shirai, *ACS Appl. Mater. Interfaces*, 2016, **8**, 31926–31934.

58 Z. Zhang, M. Wang, L. Ren and K. Jin, *Sci. Rep.*, 2017, **7**, 1–7.

59 A. E. Shalan, T. Oshikiri, S. Narra, M. M. Elshanawany, K. Ueno, H. P. Wu, K. Nakamura, X. Shi, E. W. G. Diau and H. Misawa, *ACS Appl. Mater. Interfaces*, 2016, **8**, 33592–33600.

60 G. Tang, P. You, Q. Tai, A. Yang, J. Cao, F. Zheng, Z. Zhou, J. Zhao, P. K. L. Chan and F. Yan, *Adv. Mater.*, 2019, **31**, 1–9.

61 Q. D. Yang, J. Li, Y. Cheng, H. W. Li, Z. Guan, B. Yu and S. W. Tsang, *J. Mater. Chem. A*, 2017, **5**, 9852–9858.

62 J. Troughton, K. Hooper and M. Trystan, *Nano Energy*, 2017, **39**, 60–68.

63 I. Gelmetti, N. F. Montcada, A. Pérez-Rodríguez, E. Barrena, C. Ocal, I. García-Benito, A. Molina-Ontoria, N. Martín, A. Vidal-Ferran and E. Palomares, *Energy Environ. Sci.*, 2019, **12**, 1309–1316.

64 M. A. Mahmud, N. K. Elumalai, M. B. Upama, D. Wang, B. Puthen-Veettil, F. Haque, M. Wright, C. Xu, A. Pivrikas and A. Uddin, *Sol. Energy Mater. Sol. Cells*, 2017, **167**, 87–101.

65 X. Yin, Z. Yao, Q. Luo, X. Dai, Y. Zhou, Y. Zhang, Y. Zhou, S. Luo, J. Li, N. Wang and H. Lin, *ACS Appl. Mater. Interfaces*, 2017, **9**, 2439–2448.

66 C. H. Chiang, M. K. Nazeeruddin, M. Grätzel and C. G. Wu, *Energy Environ. Sci.*, 2017, **10**, 808–817.

67 D. Luo, W. Yang, Z. Wang, A. Sadhanala, Q. Hu, R. Su, R. Shivanna, G. F. Trindade, J. F. Watts, Z. Xu, T. Liu, K. Chen, F. Ye, P. Wu, L. Zhao, J. Wu, Y. Tu, Y. Zhang, X. Yang, W. Zhang, R. H. Friend, Q. Gong, H. J. Snaith and R. Zhu, *Science (80-.).*, 2018, **360**, 1442–1446.

68 M. Saliba, J. P. Correa-Baena, C. M. Wolff, M. Stolterfoht, N. Phung, S. Albrecht, D. Neher and A. Abate, *Chem. Mater.*, 2018, **30**, 4193–4201.

69 S. Wu, Z. Li, J. Zhang, T. Liu, Z. Zhu and A. K. Y. Jen, *Chem. Commun.*, 2019, **55**, 4315–4318.

70 S. Ye, W. Sun, Y. Li, W. Yan, H. Peng, Z. Bian, Z. Liu and C. Huang, *Nano Lett.*, 2015, **15**, 3723–3728.

71 C. Zuo and L. Ding, *Small*, 2015, **11**, 5528–5532.

72 M. Wang, H. Wang, W. Li, X. Hu, K. Sun and Z. Zang, *J. Mater. Chem. A*, 2019, **7**, 26421–26428.

73 T. Liu, F. Jiang, F. Qin, W. Meng, Y. Jiang, S. Xiong, J. Tong, Z. Li, Y. Liu and Y. Zhou, *ACS Appl. Mater. Interfaces*, 2016, **8**, 33899–33906.

74 M. M. Elsenety, M. Antoniadou, N. Balis, A. Kaltzoglou, L. Sygellou, A. Stergiou, N. Tagmatarchis and P. Falaras, *ACS Appl. Energy Mater.*, 2020, **3**, 2465–2477.

75 W. Ke, C. Xiao, C. Wang, B. Saparov, H. S. Duan, D. Zhao, Z. Xiao, P. Schulz, S. P. Harvey, W. Liao, W. Meng, Y. Yu, A. J. Cimaroli, C. S. Jiang, K. Zhu, M. Al-Jassim, G. Fang, D. B. Mitzi and Y. Yan, *Adv. Mater.*, 2016, **28**, 5214–5221.

76 M. Jahandar, N. Khan, H. K. Lee, S. K. Lee, W. S. Shin, J. C. Lee, C. E. Song and S. J. Moon, *ACS Appl. Mater. Interfaces*, 2017, **9**, 35871–35879.